Doctoral Thesis

Thesis Title

Author:
Ana Andres-Arroyo

Supervisor:
Dr. First Last

A thesis submitted in fulfilment of the requirements for the degree of Doctor of Philosophy

School of Physics, Faculty of Science

August 2018

Dedicated to someone.

"Fancy Quote"

Author

Abstract

School of Physics, Faculty of Science, UNSW Australia

Doctor of Philosophy

Thesis Title

by Ana Andres-Arroyo

Write your abstract here .

Acknowledgements

The acknowledgements and the people to thank go here, don't forget to include your project advisor…

Contents

List of Figures

Abbreviations

2D Two-**D**imensional

3D Three-**D**imensional

Physical Constants

Speed of Light	c	$=$	$2.997\ 924\ 58 \times 10^{8}\ \mathrm{ms}^{-\mathrm{S}}$ (exact)
Constant Name	Symbol	$=$	Constant Value (with units)

Symbols

f	focal length	mm or cm
H	heating	K/W
I	intensity	a.u.
k	trap stiffness	pN/μm/mW
n	refractive index	—
P	power	mW
T	temperature	°C or K
ε	permittivity	???
κ	trap stiffness	pN/μm/mW
λ	wavelength	nm
μ	permeability	???
σ	cross section	???
θ	tilt angle	degrees or radians

Chapter 1

Introduction

1.1 Section title

Always put labelthesection after each section so the page headers work. [**?**]

This is a test.

1.2 Compiling instructions

1. make the main file the masted document: options -¿ make current file masted document
2. Quick build from anywhere (because it quick builds from the master document
3. BibTex from the chapter file (disable the master document option for this and do it from "normal mode")
4. Quick build 3 times (from the master document): 1 for the text, 2 for the references and labels, 3 for the bibliography backreferencing.

1.3 References

Chapter 2

Using Fourier transform phase for the measurement of radial velocity

This chapter introduces a new method for measuring radial velocities. Specifically, it uses the Fourier transform of a line profile (or cross-correlation profile) to try and distinguish between the effects of a bulk shift in that profile (i.e. a radial velocity shift of the profile), opposed to a change in the line profile shape which can produce an apparent radial velocity shift. We examine the impact on the Fourier transformed components of a line profile of both bulk line shifts, and line profile deformations, with the aim of developing tools to distinguish between these two cases.

2.1 Phase analysis of Fourier transform for the measurement of line shift

2.1.1 Translation property of Fourier transform

The translation of a function (in our case a spectral line profile) can be examined in both its original real space, and in its Fourier transformed space. Because Fourier techniques are often used to handle time domain data, this shift in real space can be variously considered described as either time shifting or translation. In this chapter we will use "time shifting", "translation" and "velocity shifting" interchangeably to refer to a shift of a function in real space. We will refer to Fourier transformed functions as being in the "frequency domain" regardless of whether they have actual dimensions of 1/time, 1/length or 1/velocity.

Let us consider a function $h(x)$ be a signal $f(x)$ delayed (or shifted) by an amount x_0:

$$h(x) = f(x - x_0). \tag{2.1}$$

In the frequency domain, we will then have

$$\hat{h}(\xi) = e^{-2\pi i x_0 \xi} \hat{f}(\xi), \tag{2.2}$$

where the circumflex denotes the Fourier transform of a function. $\hat{h}(\xi)$ and $\hat{f}(\xi)$ will therefore differ by a frequency dependent phase angle:

$$\Delta\phi(\xi) = -2\pi x_0 \xi, \tag{2.3}$$

while the power spectral density will remain unchanged (as $\mid e^{-2\pi i x_0 \xi} \mid^2 = 1$).

2.1.2 Intuitive explanation

The translation property of the Fourier transform follows mathematically from the nature of the transform. A (perhaps) more intuitive way to see this is that since the Fourier transform is defined

$$\hat{f}(\xi) = \int_{-\infty}^{\infty} f(x)e^{-2\pi i x\xi}dx, \tag{2.4}$$

it decomposes the function $f(x)$ into a frequency representation $\hat{f}(\xi)$, such that the function $f(x)$ is expressed as the sum of *all* the orthogonal basis $e^{2\pi i x\xi}$ times a set of their components $\hat{f}(\xi)$ (i.e. by the inverse Fourier transform):

$$f(x) = \int_{-\infty}^{\infty} \hat{f}(\xi)e^{2\pi i x\xi}d\xi. \tag{2.5}$$

This means that shifting $f(x)$ by x_0 is equivalent to shifting *all* the orthogonal basis functions by x_0, which becomes $e^{2\pi i(x-x_0)\xi} = e^{2\pi i x\xi} \cdot e^{-2\pi i x_0\xi}$. This is how the $e^{-2\pi i x_0\xi}$ term in Eq. 2.2 arises – it quantifies this phase difference. [1]

The fact that the power spectrum density remains the same can also intuitively seen, because shifting the signal as a whole doesn't add or remove any frequency information.

2.1.3 Practical Use

From Eq. 2.3, we see that the phase shift $\Delta\phi(\xi)$ is proportional to the frequency ξ with a constant gradient or slope [2]

$$\frac{\mathrm{d}(\Delta\phi)}{\mathrm{d}\xi} = -2\pi x_0 \tag{2.6}$$

Obtaining this (in principle) is straightforward via a simple linear regression model fit to a plot of $\Delta\phi(\xi)$ versus ξ (see e.g. Fig. 2.1), so that

$$x_0 = -\frac{1}{2\pi}\frac{\mathrm{d}(\Delta\phi)}{\mathrm{d}\xi} \tag{2.7}$$

[1] For a simplified vision bridging a shift of the signal in the time domain and a phase difference in the frequency domain, imagine any real continuous function is a sum of sines and cosines. Changing the phase angle in the sines and cosines results in shifts in the function.

[2] We use Δ to refer to the phase difference between a shifted line profile and a unshifted / referenced line profile, while the derivative to refer to the response of $\Delta\phi$) to ξ.

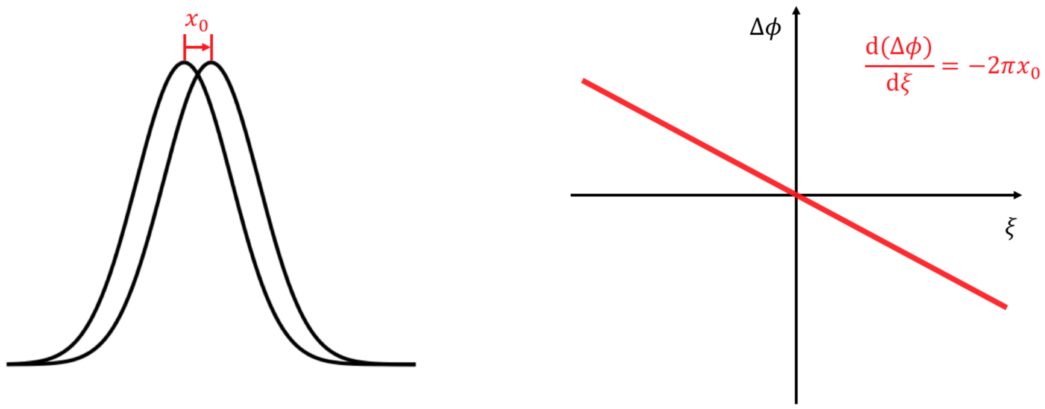

Fig. 2.1: The left panel shows a signal (or a spectral line profile in the following context) shifted by an amount x_0. The right panel is the differential phase spectral density diagram (i.e. differential phase spectrum). The model shows a perfectly linear correlation between $\Delta\phi(\xi)$ and ξ with the constant slope $-2\pi x_0$.

By analogy with the definition of power spectral density, we describe $\phi(\xi)$ the "phase spectral density" and hence $\Delta\phi(\xi)$ the "differential phase spectral density".

In principle then, an analysis of the phase shift in the frequency domain of the Fourier components of a line profile will provide a means of measuring a bulk line shift in real space.

2.1.4 Initial tests

We performed an initial test to determine whether we can correctly recover known shifts of a line profile from an analysis of the phase shift in the frequency domain of the Fourier transform of shifted line profiles.

We generated a spectral line profile based on the cross-correlation function of observed HARPS spectra with the software SOAP 2.0 [1]. This was replicated 100 times, with a very small amount of noise (equivalent to a S/N = 10,000) injected in each of the line profiles. These profiles were then subjected to radial velocity shifts evenly spaced between 0 and 10 m/s (Fig. 2.2).

The Fourier transform of these 100 spectral line profiles divides the information into two parts: (1) the power spectra (Fig. 2.3a) and (2) the phase spectra (shown in Fig. 2.3b as the differential phase spectra relative to the phase spectrum for the unshifted line profile).

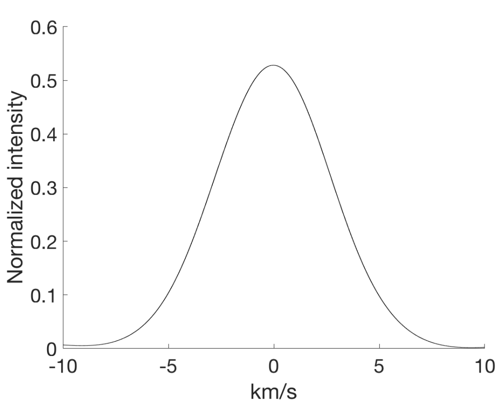

(a) Line profile (stacked)

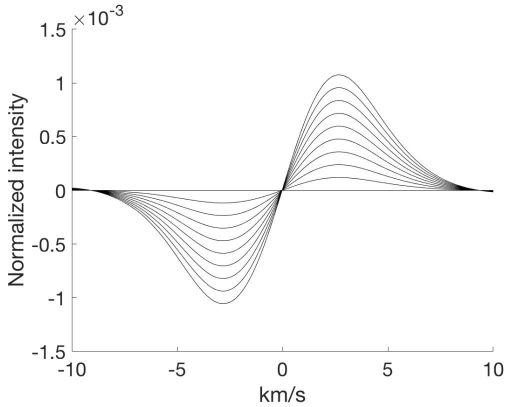

(b) Differential line profile

Fig. 2.2: (a) the shifted line profiles plotted on top of each other, showing that the ±0-10 m/s shifts are very small compared to the line profile width. (b) the shifted line profiles with the unshifted line profile subtracted from each. Note that for demonstration clarity, noise is not included in this differential line profile plot and only 10 out of 100 profiles are presented.

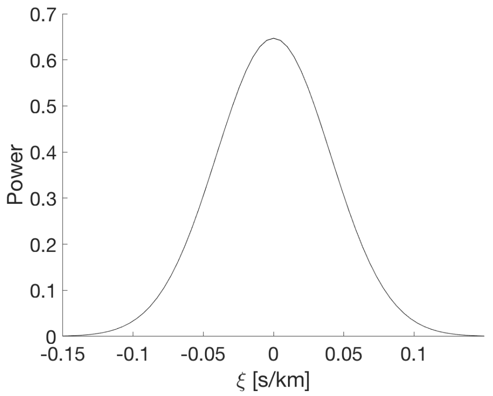

(a) Power spectrum (stacked)

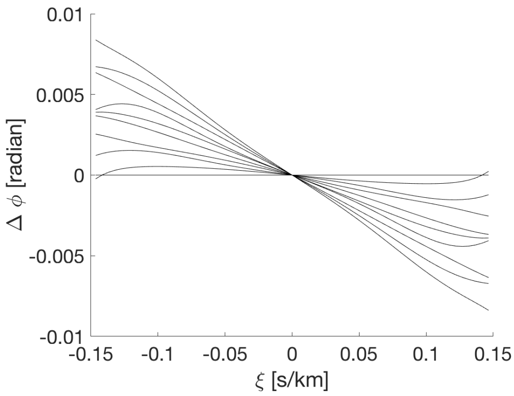

(b) Differential phase spectrum

Fig. 2.3: The Fourier transform of these shifted line profile divides the information in each into (a) their power spectra and (b) their phase spectra (here plotted differential compared to that of the unshifted profile). A line shift in the time domain produces an unchanged power spectrum in the frequency domain. It does, however, produce phase shift which we see as linear trends in the differential phase spectra as a function of frequency. Note that for demonstration clarity, only 10 out of 100 differential phase spectra are presented.

We see that most Fourier transform information is concentrated towards the centre of the power spectrum (i.e. the lower frequency range). The differential phase spectra are expected linear (as Fig. 2.1 demonstrated). Its deviation from linearity comes from the noise that we injected, which will be discussed later.

The slope of each differential phase spectrum indicates the shift of each line profile relative to the unshifted line profile. It should be weighted by the amplitude of the power, meaning the lower frequencies are higher weighted. We therefore calculate the radial velocity shift for each shifted line profile using two methods:

1. the RV_{FT} using Eq. 2.7, weighted by the power spectrum
2. the RV_{Gaussian} as traditionally measured from the line centroid by fitting a Gaussian to each line profile.

We can then compare the results with the (known) input line shift where we see the expected strong 1:1 correlation (Fig. 2.4)[3]. The root-mean-square (rms) of the residuals are both $rms_{\mathrm{FT}} = rms_{\mathrm{Gaussian}} = 0.08$ m/s, identical up to two decimal places, indicating the expected radial velocities are consistently reduced. In fact, the almost overlapping residual in Fig. 2.4 means that the two methods are so coherently different from the input radial velocity (by a small amount), concludes that such a deviation comes from the photon noise intrinsic to the line profile rather than the methods themselves.

CGT: How do these comare which what you'd expect from the S/N and the intrinsic line width (should say at some int what the intrinsic line width is.

[3]The line of best fit presents a slope of 1.002 ± 0.006 with 95% confidence bounds. The uncertainty of the slope is derived from the uncertainty of each measured RV_{FT}, which is further derived from the uncertainty of the phase measurement, described by the magnitude of the power spectrum.

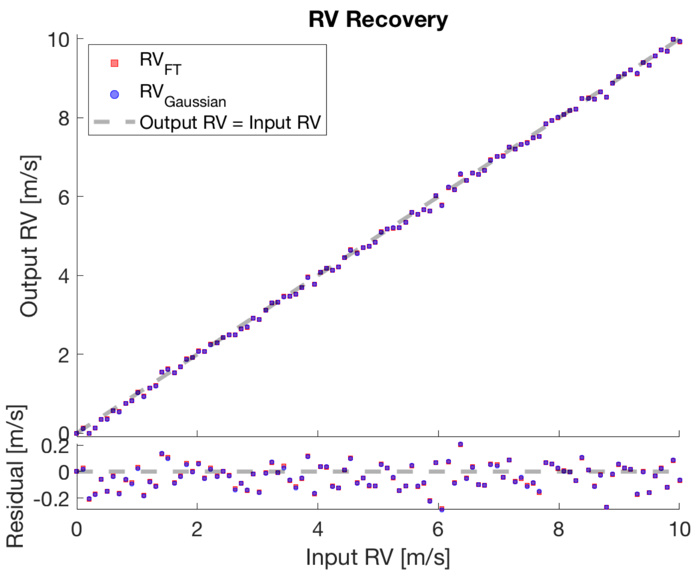

Fig. 2.4: Radial velocity recovery of line shifts with both methods: Fourier transform and Gaussian fit. Both results are highly consistent with each other. Errorbars are not plotted for clarity.

2.1.5 Further tests

Let's recall the justification of measuring a line shift in its Fourier space – the shifting of a line (or a function), when viewed as shifting the sum of its Fourier basis functions (or any other basis functions), has equally the same amount of shift on every basis function, which can be measured as a phase shift in the Fourier phase spectrum. That is to say, utilising only part of the phase spectrum will also return the correct amount of shift of a line profile, although it is more likely to be affected by noise. The motivation of this practice will be discussed in §2.2 when it comes to line profile deformations, while we simply lay out the tests in this subsection.

We choose to divide the whole frequency range into two parts (Fig. 2.5) – the lower frequency range (i.e. apply a low-pass filter) and the higher frequency range (i.e. apply a high-pass filter). The dividing frequency ξ_{HL} is chosen such that both the lower and higher frequency ranges take up half of the power spectrum:[4]

$$\int_0^{\xi_{HL}} P(\xi)d\xi = \int_{\xi_{HL}}^{+\infty} P(\xi)d\xi, \tag{2.8}$$

[4]In practice, a cut-off frequency applies to the upper boundary of the high-pass filter. Frequencies higher than the cut-off frequency hardly contributes to the shape of the line profile as the power goes to 0, and they can be impacted by noise in a unpredictable way, although they are weighted by the nearly-zero power.

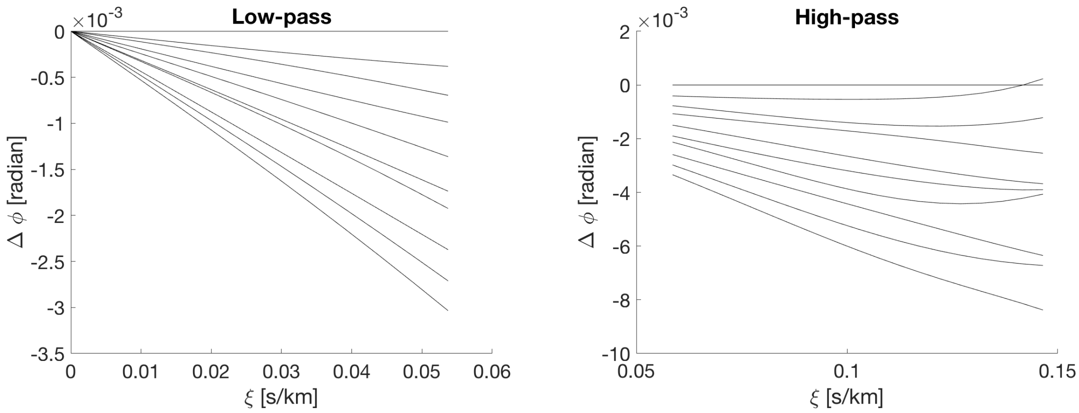

Fig. 2.5: Differential phase spectrum as shown in Fig. 2.3b sub-divided into lower frequency range and higher frequency range. Only the non-negative ranges are plotted.

assuming the integration of power spectrum is a measurement of the amount of "information", so that in a noise-free circumstance, we would put equal trust on the radial velocities obtained from the lower and higher frequencies. In the following, we use $RV_{\mathrm{FT,L}}$ and $RV_{\mathrm{FT,H}}$ to represent these two radial velocities.

Similar to Fig. 2.4 where we make use of the full range of frequencies, Fig. 2.6 also presents a good 1:1 alignment between $RV_{\mathrm{FT,L}}$, $RV_{\mathrm{FT,H}}$ and the input radial velocity[5]. The root-mean-square (rms) of the residuals are $rms_{\mathrm{FT,L}} = 0.13$ m/s and $rms_{\mathrm{FT,H}} = 0.48$ m/s, seemingly contradicting with the expectation that equal amount of "information" from which $RV_{\mathrm{FT,L}}$ and $RV_{\mathrm{FT,H}}$ are derived should deliver the same rms. The answer lies in the impact of noise (§2.1.6) – higher frequency modes are more likely to be subjected to line deformations arising from stochastic behaviours, such as photon noise, stellar variability...

[5]The line of best fit presents a slope of 1.004 ± 0.008 for $RV_{\mathrm{FT,L}}$ and 1.009 ± 0.029 respectively, with 95% confidence bounds.

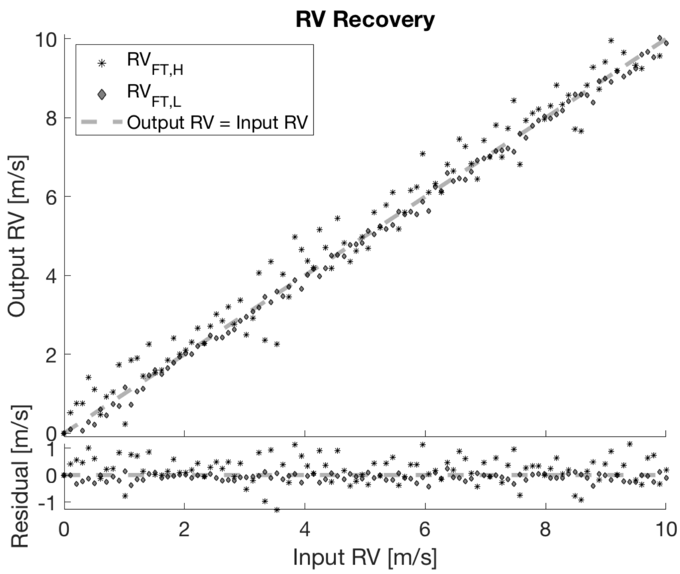

Fig. 2.6: Radial velocity recovery of line shifts with low-pass and high-pass filters. Errorbars are not plotted for clarity.

2.1.6 Cut-off frequency

We briefly mentioned in §2.1.4 that the deviation from linearity in the differential phase spectrum arises from the photon noise injected in the simulated line profile, and in §2.1.5 that introducing a cut-off frequency in the upper boundary avoids dealing with excessive noise. This can be explained with the Fourier transformed line profile $\hat{h}(\xi)$ in a complex plane (also known as the Argand plane; Fig. 2.7). What we see is $\hat{h}(\xi)$ literally plotted on the complex plane – of each complex number $\hat{h}(\xi)$, the argument returns the phase angle and the square of the absolute value returns the power, for that particular frequency ξ. For larger powers (i.e. $\hat{h}(\xi)$ far from the origin), the presence of noise hardly alters the phase angle; for lower powers (i.e. $\hat{h}(\xi)$ distributed in the vicinity of the origin), a slight displacement of $\hat{h}(\xi)$ in the complex plane means a considerable change in the phase angle. It justifies using the Fourier transform spectral power to be the weight of each frequency, and introducing a cut-off frequency when making a linear fit of the differential phase spectrum.

Another possible reason for introducing the cut-off frequency is the periodicity of the basis functions in a Fourier transform. The basis function $e^{-2\pi i x_0 \xi}$ repeats itself at the period of $1/\xi$, making measuring the shift longer than the order of $1/\xi$ degenerate because $x_0 + k/\xi$ for $k \in \mathbb{Z}$ will give the same results. However, this is very unlikely the case that we may encounter. In the test examples above, the cut-off frequency is

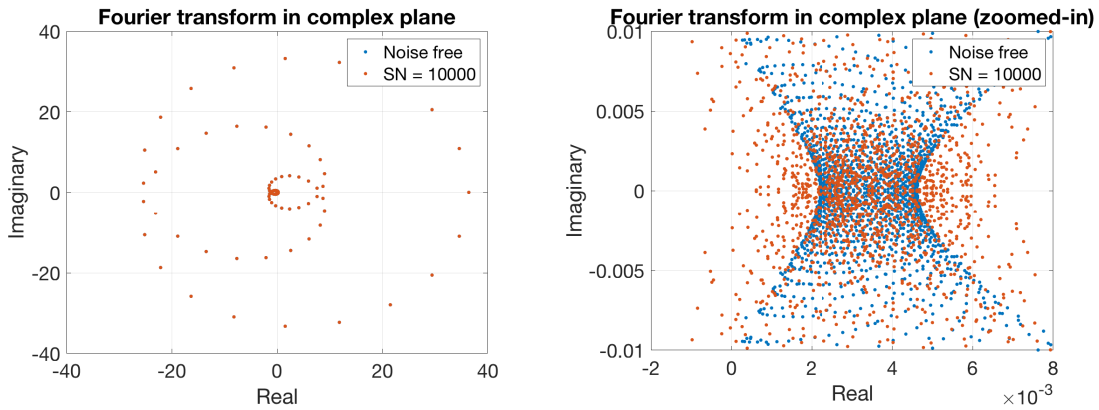

Fig. 2.7: The Fourier transform of a line profile in a complex plane. The right figure is a zoom-in of the left near the origin.

$\xi = 0.15$ s/km, corresponding to the period of $1/\xi \sim 6.7$ km/s, way larger than the radial velocities induced by planets at m/s amplitudes.

2.1.7 Conclusion

In this section, we have introduced a new method for measuring radial velocities – Fourier phase spectrum analysis. The tests that we have made based on shifting a simulated line profile confirm our expectation that using the differential Fourier phase spectrum, it is possible to measure a radial velocity to similarly high precision. This provides an alternative to the traditional means of obtaining the radial velocities via centroiding the line profile in real space.

In a broader context, this method will be applicable to measuring shifts of any pattern, and can be extended to higher dimensions. In this thesis, we primarily focus on its use to measure radial velocity shifts in spectral line profiles, and especially whether the Fourier transform phase velocity is more robust against the influence of changes in line deformation than traditional techniques.

2.2 Using the Fourier transform to probe line deformation

In § 2.1, we have tested that the Fourier phase spectrum analysis correctly measures the actual line profile shifts due to a bulk motion of the emitting star. In this section, we wish to test whether this method is more robust against spurious apparent radial velocity shifts produced by changes in the line profile shape in an emitting stars.

2.2.1 Theory

For a shift of a line profile by a small amount x_0, the same shift x_0 applies to *all* of its basis functions. As for line deformation due to stellar variability, x_0 becomes frequency dependent [6]. That is to say, basis functions at different frequencies would be shifted by different amounts, resulting in shape changes (e.g. skewness) in the line profile. Therefore we modify the translation property of Fourier transform by rewriting x_0 as $x_0(\xi)$ in Eq. 2.3:

$$\Delta\phi(\xi) = -2\pi x_0(\xi)\xi. \tag{2.9}$$

As a result, the local gradient of the differential phase spectrum becomes

$$\frac{\mathrm{d}(\Delta\phi)}{\mathrm{d}\xi} = -2\pi(x_0 + \frac{\mathrm{d}x_0}{\mathrm{d}\xi}), \tag{2.10}$$

which reduces to Eq. 2.6 when x_0 is a constant as in the case of a bulk line shift. Note that the dependency of ξ has been taken out of $\Delta\phi(\xi)$ and $x_0(\xi)$ in writing the differential equation above.

In principle, we could numerically solve this differential equation based on the measured local gradient $\mathrm{d}(\Delta\phi)/\mathrm{d}\xi$ to obtain $x_0(\xi)$, but this local gradient measurement can be unreliable in the presence of noise. As a simplistic approach, we could use the *averaged* shift $\overline{x_0(\xi)}$ of various frequency modes to describe different amounts of shift by rewriting Eq. 2.9 as

$$\Delta\phi(\xi) = -2\pi\overline{x_0(\xi)}\xi \tag{2.11}$$

where $\overline{x_0(\xi)}$ is treated as a constant. This concept will be helpful in describing the effective shifts applying the low-pass and high-pass filters when it comes to line deformation.

2.2.2 SOAP Simulations

With SOAP 2.0, we injected three spots with different longitudes, latitudes and sizes (parameters specified in Table 2.1) to model an emitting star, and generated 100 cross-correlation functions for the resulting deformed line profiles evenly sampled throughout

[6] excluding the case where the result of a line deformation is exactly the same as a line shift, as this becomes indistinguishable by any means of studying the shape of the line profile alone

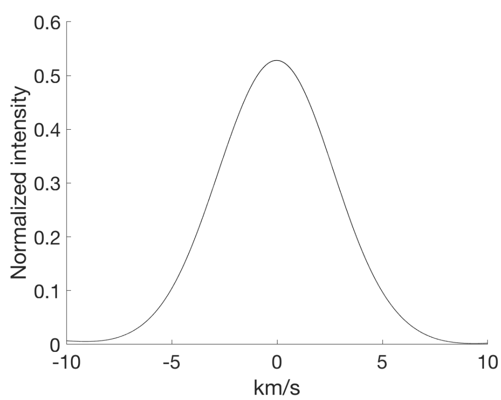

(a) Line profile (stacked)

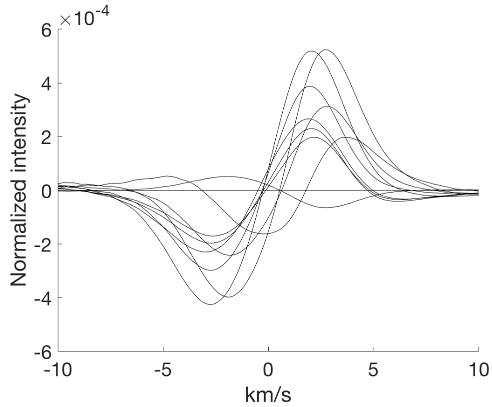

(b) Differential line profile

Fig. 2.8: Deformed line profile. For the sake of clarity, noise is not included in the differential line profile plot and only 10 out of 100 profiles are presented.

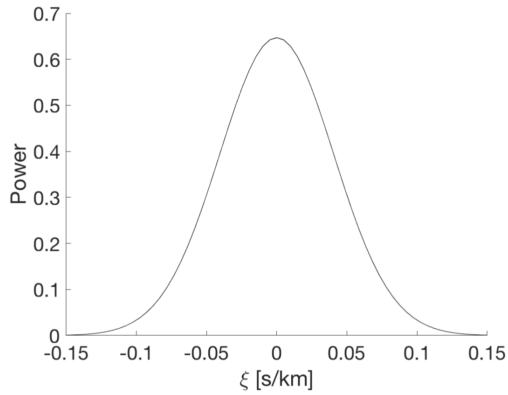

(a) Power spectrum (stacked)

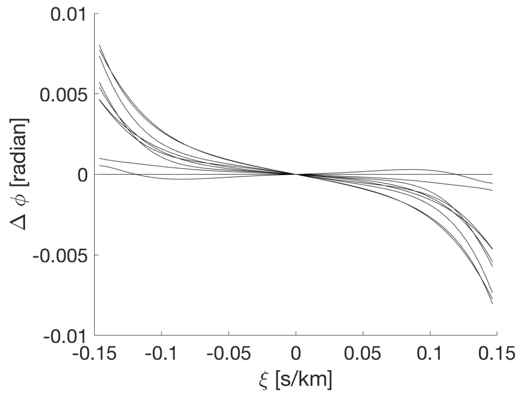

(b) Differential phase spectrum

Fig. 2.9: Fourier transform of deformed line profile. Only 10 out of 100 differential phase spectra are presented.

the rotation period of the star (Fig. 2.8). A very small amount of noise (equivalent to a S/N = 10,000) was also added into the line profiles. We then take the same approach as in § 2.1 to obtain the power spectrum and (differential) phase spectrum (Fig. 2.9) to recover the radial velocities RV_{FT}. It notes, line deformation contributes to a skewed differential phase spectrum, as predicted in §2.2.1.

	Longitude	Latitude	Size in disk area percentage
Spot 1	174°	-14°	0.18%
Spot 2	288°	74°	0.40%
Spot 3	51°	52°	0.50%

Table 2.1: Spot configurations

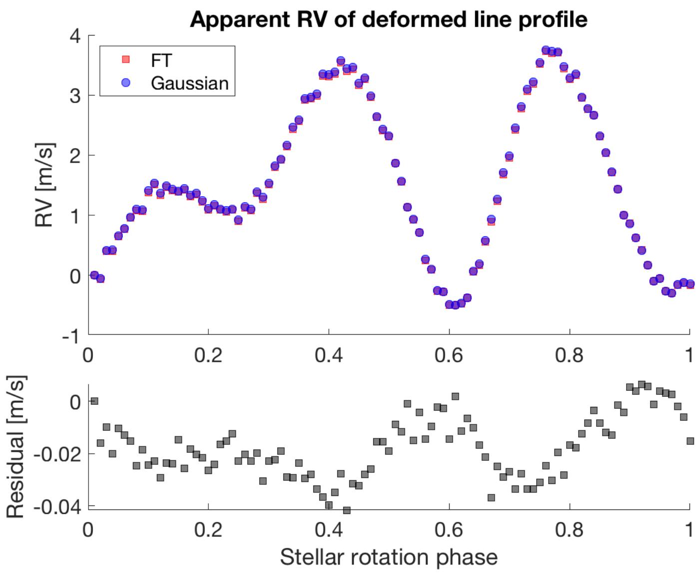

Fig. 2.10: Apparent RV of deformed line profile calculated with Fourier transform and Gaussian fit. Both results are also highly consistent with each other.

In this case, the input radial velocities would be the apparent radial velocities of deformed line profiles (also known as jitter). Both velocities RV_{FT} and RV_{Gaussian} are plotted against rotation phase (Fig. 2.10). If we take the root-mean-squares of both RV_{FT} and RV_{Gaussian} to be the intrinsic noise level ($rms_{\mathrm{FT}} = rms_{\mathrm{Gaussian}} = 0.08$ m/s) corresponding S/N = 10,000, the uncertainty of $RV_{\mathrm{FT}} - RV_{\mathrm{Gaussian}}$ as residual would have an uncertainty of $\sqrt{rms^2_{\mathrm{FT}} + rms^2_{\mathrm{Gaussian}}} \approx 0.11$ m/s, meaning that the residuals are 0 within uncertainty and showing that RV_{FT} and RV_{Gaussian} are indistinguishably consistent.

Remark Using (almost) all the information in the power spectrum and the phase spectrum will end up with the same radial velocity as acquiring the line centroid fitted by a Gaussian line profile.

Although the intrinsic line deformation (in the absence of any velocity shift in the host star) does mimic the radial velocity shift, we note the shape and scale differences in the differential phase spectrum between an actual line shift (Fig. 2.3) and a line deformation (Fig. 2.9) – the latte becomes highly skewed as $\mid \Delta\phi \mid$ increases dramatically towards higher frequencies. Such differences provide key messages to differentiate the two circumstances.

...

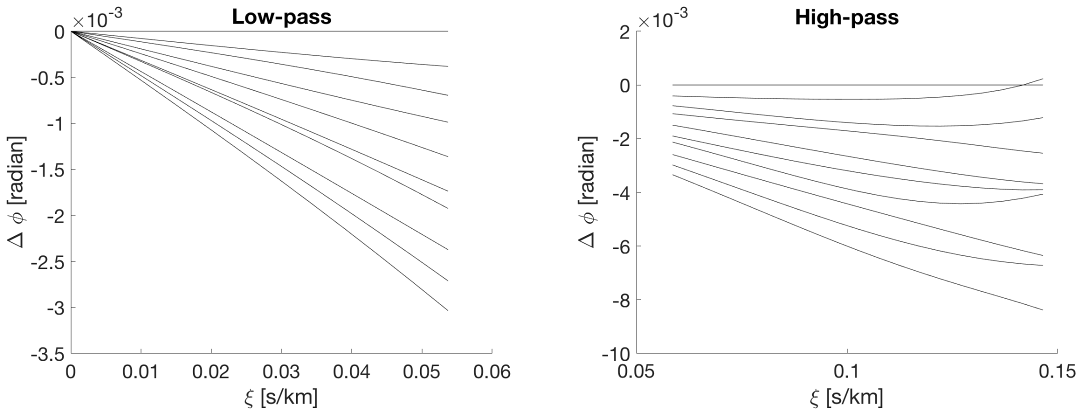

Fig. 2.11: Differential phase spectrum as shown in Fig. 2.9b sub-divided into lower frequency range and higher frequency range. Only the non-negative ranges are plotted.

and compute the equivalent Fourier transformed radial velocity RV_{FT} for each, we would obtain two sets of radial velocities, one represents the radial velocity shifts (denoted as $RV_{\mathrm{FT,L}}$) of the lower frequency components and the other (denoted as $RV_{\mathrm{FT,H}}$) represents the higher.

We find, to our surprise, that both $RV_{\mathrm{FT,L}}$ and $RV_{\mathrm{FT,H}}$ are linearly correlated with the jitter (equivalent to RV_{Gaussian} in this case as no planets are present; Fig. 2.12), yet neither has a 1:1 correlation – $RV_{\mathrm{FT,H}}$ demonstrates a higher response to jitter, with a slope $k_{\mathrm{H}} = 1.8599$ in the linear fit, meaning the radial velocity shift of 1 m/s due to line deformation is detected as 1.8599 m/s shift on average using *this* high-pass filter; whereas $k_{\mathrm{L}} = 0.8245$ for $RV_{\mathrm{FT,L}}$, meaning such a 1 m/s deformation is detected as 0.8245 m/s shift on average using *this* low-pass filter. When we combine both filters, we would have obtained the 1:1 correlation as discussed above (Fig. 2.10).

We could further investigate how well this linearity behaves for each filter by scaling the measured $RV_{\mathrm{FT,L}}$ and $RV_{\mathrm{FT,H}}$ by their corresponding factors $1/k_{\mathrm{L}}$ and $1/k_{\mathrm{H}}$ respectively, and compare them with the jitter (RV_{Gaussian}), as presented in Fig. 2.13. The root-mean-squares of the residuals ($RV_{\mathrm{FT,L/H}} - RV_{\mathrm{Gaussian}}$) are $rms_{\mathrm{FT,L}} \approx 0.15$ m/s and $rms_{\mathrm{FT,H}} \approx 0.32$ m/s respectively. Not surprisingly, $rms_{\mathrm{FT,H}} > rms_{\mathrm{FT,L}}$, because in *this* case more information is concentrated in the low-pass filter (i.e. $\int_0^{0.05} \mid P \mid d\xi > \int_{0.05}^{0.15} \mid P \mid d\xi$ where P is the amplitude of the power spectrum). For this reason, $rms_{\mathrm{FT,L}} - RV_{\mathrm{Gaussian}}$ would be more stable and less scattered. If the bound between the low- and high-pass filer ξ_0 is chosen such that $\int_0^{\xi_0} \mid P \mid d\xi = \int_{\xi_0}^{0.15} \mid P \mid d\xi$, we would expect $rms_{\mathrm{FT,H}} = rms_{\mathrm{FT,L}}$.

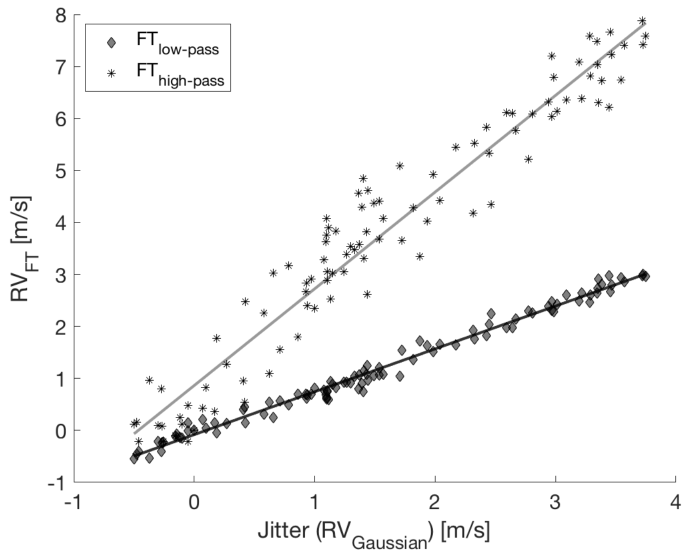

Fig. 2.12: Applying the low-pass and high-pass filters, the Fourier transform $RV_{\mathrm{FT,L}}$ and $RV_{\mathrm{FT,H}}$ are linearly correlated with the jitter (RV_{Gaussian}).

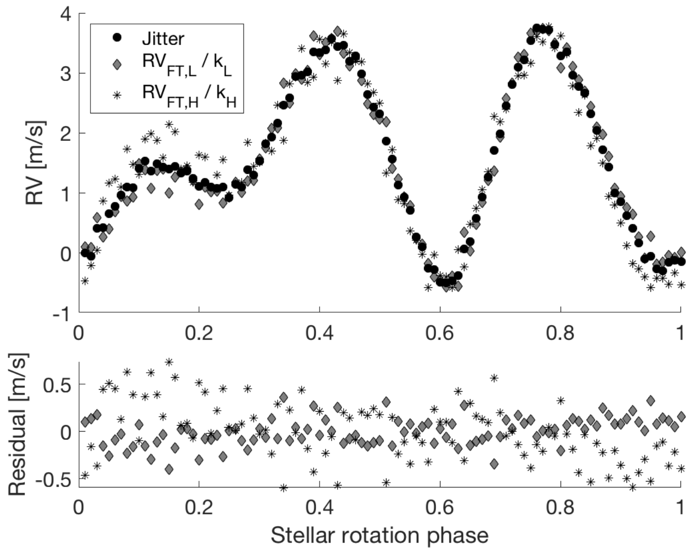

Fig. 2.13: Scaling the low-pass and high-pass Fourier transformed radial velocities to match the input jitter.

18

Remark The apparent radial velocity shift due to spectral line deformation (i.e. jitter) can be seen as a mingle of one radial velocity shift in higher frequency components and one in lower frequency components. They are both, in the SOAP simulations, scaled with the jitter.

2.2.3 Jitter model

We have found in § 2.1 that $RV_{\rm FT}$ and $RV_{\rm Gaussian}$ demonstrate basically the same response to line shifts. For its linearity in the differential phase spectrum as a result of a line shift (Fig.2.3b), we can interpolate the conclusion to part of the differential phase spectrum, that is, both $RV_{\rm FT,H}$ and $RV_{\rm FT,L}$ will also have the same response as $RV_{\rm Gaussian}$ to a line shift. We have also found earlier in this section (§ 2.2) that $RV_{\rm FT,L}$ *CGT: What range compared to, say, the line width of the line profile?* is less sensitive ($k_{\rm L} = 0.8245$) to line deformation than $RV_{\rm Gaussian}$, whereas $RV_{\rm FT,H}$ is more sensitive ($k_{\rm H} = 1.8599$).

We can therefore write the following measurable quantities – $RV_{\rm FT,L/H}$ and $RV_{\rm Gaussian}$ – as the sum of corresponding contributions from a bulk shift in the star (which we hereafter assume to be due to a planet or planets), and variability in the stellar line profile (hereafter lumped under the general name "jitter"):

$$RV_{\rm Gaussian} = RV_{\rm planet} + RV_{\rm jitter}$$

$$RV_{\rm FT,L} = RV_{\rm planet} + k_L \cdot RV_{\rm jitter} \tag{2.12}$$

$$RV_{\rm FT,H} = RV_{\rm planet} + k_H \cdot RV_{\rm jitter}. \tag{2.13}$$

Subtracting one from the other to remove $RV_{\rm planet}$ gives

$$RV_{\rm Gaussian} - RV_{\rm FT,L} = (1 - k_L) \cdot RV_{\rm jitter} \tag{2.14}$$

$$RV_{\rm Gaussian} - RV_{\rm FT,H} = (1 - k_H) \cdot RV_{\rm jitter} \tag{2.15}$$

$$RV_{\rm FT,H} - RV_{\rm FT,L} = (k_H - k_L) \cdot RV_{\rm jitter}. \tag{2.16}$$

Note that only (any) two of them are independent equations, as the any one can be derived from the other two. Rearranging also yields two out of three independent expressions for the jitter model

$$RV_{\text{jitter}} = \frac{RV_{\text{Gaussian}} - RV_{\text{FT,L}}}{1 - k_L} \tag{2.17}$$

$$RV_{\text{jitter}} = \frac{RV_{\text{Gaussian}} - RV_{\text{FT,H}}}{1 - k_H} \tag{2.18}$$

$$RV_{\text{jitter}} = \frac{RV_{\text{FT,H}} - RV_{\text{FT,L}}}{k_H - k_L} \tag{2.19}$$

where $RV_{\text{Gaussian}}, RV_{\text{FT,L}}$ and $RV_{\text{FT,H}}$ are direct measurements, whereas k_L and k_H are unknowns but can be incorporated into the radial velocity models (Eq. 2.12 and Eq. 2.13) in the process of recovering planets. When there's no planet or the planetary radial velocity signal is negligible compared with the size of jitter, $RV_{\text{FT,L}}$ and $RV_{\text{FT,H}}$ will be proportional to RV_{jitter} (Example: §2.3.1).

2.2.4 Testing the recovery of Jitter

We again performed tests to see if we can correctly recover artificially generated model jitter using our new technique (Eq. 2.17 to Eq. 2.19).

We generated 200 deformed line profiles (in the form of cross-correlation functions) using SOAP 2.0. All the configurations are the same as used in §2.2.2, except that they are evenly sampled throughout two rotation periods. The jitter amplitude is roughly 2 m/s. In addition, each line profile is further shifted by an amount RV_{planet} appropriate for a planet generating a Keplerian orbit in the star of the amplitude

$$A_{\text{planet}} = 2 \text{ m/s}$$

and a planetary orbital period to stellar rotation period ratio of 0.7;

$$\frac{\nu_{\text{orb}}}{\nu_{\text{rot}}} = \frac{P_{\text{rot}}}{P_{\text{orb}}} = 0.7.$$

In principle, the RV_{planet} configuration shouldn't matter much because it will be mostly cancelled out *CGT: cancelled? Or swamped?* in the jitter model.

We then obtain two sets of radial velocities for each simulated profile: RV_{Gaussian} and RV_{FT}, which are reproduced in the upper panel of Fig. 2.14. As we know the amount of input jitter in our simulation, we simply scale up ΔRV by a parameter α to match the input jitter (dashed line in middle panel). *CGT: You've lost me here ...* The jitter model (black dots in middle panel) becomes more scattered as $\alpha \gg 1$. As a result, a moving average modulated by a Gaussian kernel is implemented to smooth out the data (solid line in middle panel).

CGT: I'm confused - whats the difference between input jitter and model jitter?

To examine the performance, we compare the rms of the input jitter rms_{jitter} and the rms of the residual between the input jitter and the model jitter rms_{residual}. The former can be treated as the scatter after fitting the correct planet(s) without jitter correction, while the latter can be treated as the scatter after the additional jitter is removed. The rms *CGT: of what? which one?* is reduced from $rms_{\text{jitter}} = 1.22$ m/s to $rms_{\text{residual}} = 0.70$ m/s, which is crucial in enhancing the detection of planets with radial velocities of sub-m/s amplitudes. However, we should also note that there are systematic differences between the input jitter and our model jitter (i.e. the residual sorts of repeats itself in the two stellar rotation periods).

We should be aware that while removing the stellar variability contribution from the data, it may also add in some remnant features. *CGT: I'm afraid this is a sort of meanngless statement.*

2.2.5 End-to-end Simulations

Unless we are sure of a null-planetary system where $RV_{\text{planet}} = 0$ and from Eq. **??** and Eq. **??** we obtain

$$k = RV_{\text{jitter}}/RV_{\text{Gaussian}}, \tag{2.20}$$

normally k cannot be directly calculated, so neither can α be. However, we could substitute the jitter model (Eq. **??**) into Eq. **??**, such that

$$RV_{\text{Gaussian}} = RV_{\text{planet}} + \alpha \cdot \Delta RV \tag{2.21}$$

where RV_{planet} is parametrised by Keplerian orbit(s) and both RV_{Gaussian} and ΔRV are measurable.

The tests are divided into two groups for comparison:

1. Fit RV_{Gaussian} by Keplerian orbit alone;
2. Fit RV_{Gaussian} by Keplerian orbit + jitter model (i.e. $\alpha \cdot \Delta RV$).

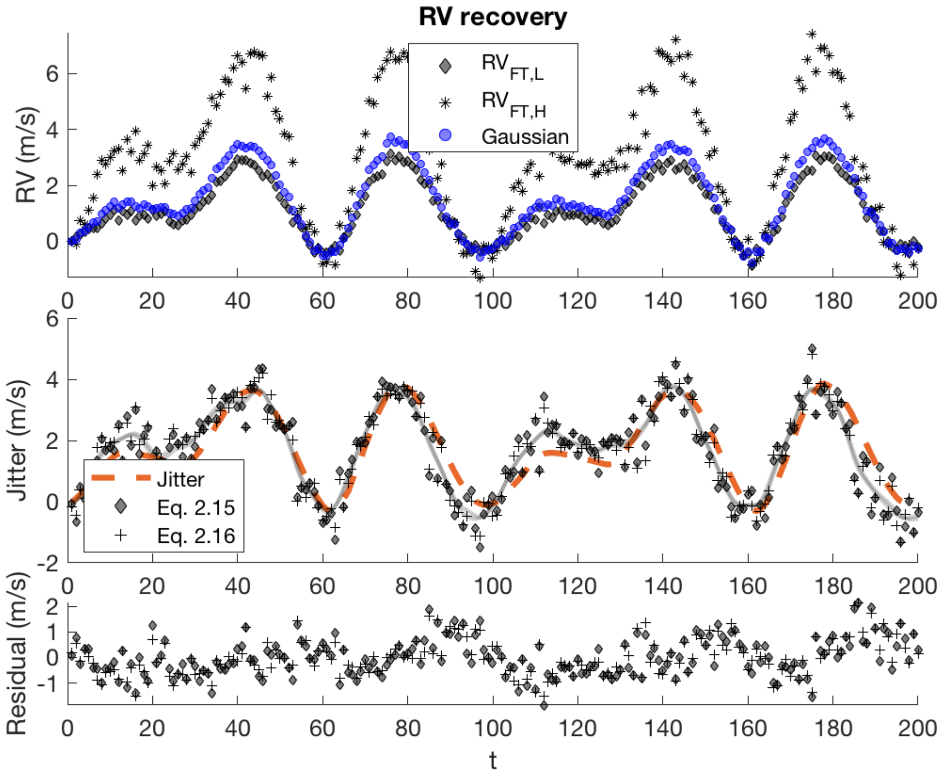

Fig. 2.14: Construct jitter model from simulation data.

The injected planet has the same parameter settings as in §2.2.4, i.e. circular orbit with amplitude $A = 2$ m/s, orbital frequency ratio $\nu = 0.7$ and initial phase $\omega = 1$ rad. We will compare which group recovers the planet parameters better.

To better simulate the real observations, 40 data samples out of 200 from the two rotation periods are randomly selected. The fitting is achieved by running MCMC to maximise the log-likelihood function given the model. For the simulation, each radial velocity data is equally weighted (as they have the same S/N). It is defined if the input parameter lies within 1σ errorbar of the output parameter, it counts as a successful detection.

For demonstration, we show one of the outputs in corner plots (Fig. 2.15) and the corresponding radial velocity fitting (Fig. 2.16). The corner plot visually shows the how the walkers explore the parameter space and their distribution. The histogram gives an example explaining how a "successful detection" is qualified. The radial velocity fitting plot demonstrates an example that implementing the jitter model effectively accounts

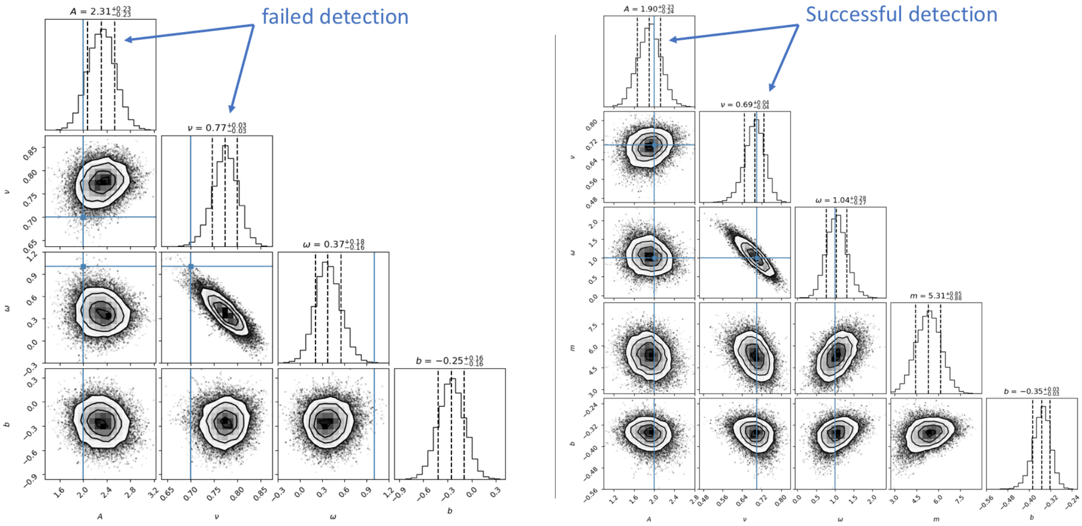

Fig. 2.15: Corner plots of MCMC. Theses are two examples of the output of MCMC: no jitter correction on the left and with jitter correction on the right. The input parameters are highlighted in the blue solid line. The three dashed lines of each histogram indicate the median and 1σ on both sides. On the left panel both blue lines of A and ν are outside the 1σ region, therefore it counts as a "failed detection"; on the right panel, it counts as a successful detection within 1σ.

for the spurious signals in the raw radial velocity data, reducing the rms from 1.14 m/s to 0.55 m/s.

In the end, we run 100 trails for the end-to-end simulation. The random differences among these 100 trails come from:

- photon noise given the S/N;
- randomly selected 40 samplings in the 200 line profiles.

It turns out that in 46% of the 100 trails are successful detections for both A and ν when we apply the jitter correction model, while this percentage is only 11% without jitter correction. In more detail, Fig. 2.17 shows that with jitter correction (in red), both of the amplitude and orbital frequency ratio tend to be underestimated, which is shown opposite for the results without correction (in blue). Moreover, the jitter corrected parameters are better constrained (i.e. with narrower distributions) and performs much better in ν than without correction. While it is tempting to say the correct answer is more likely in between the results from these two fittings, we would need more tests to conclude.

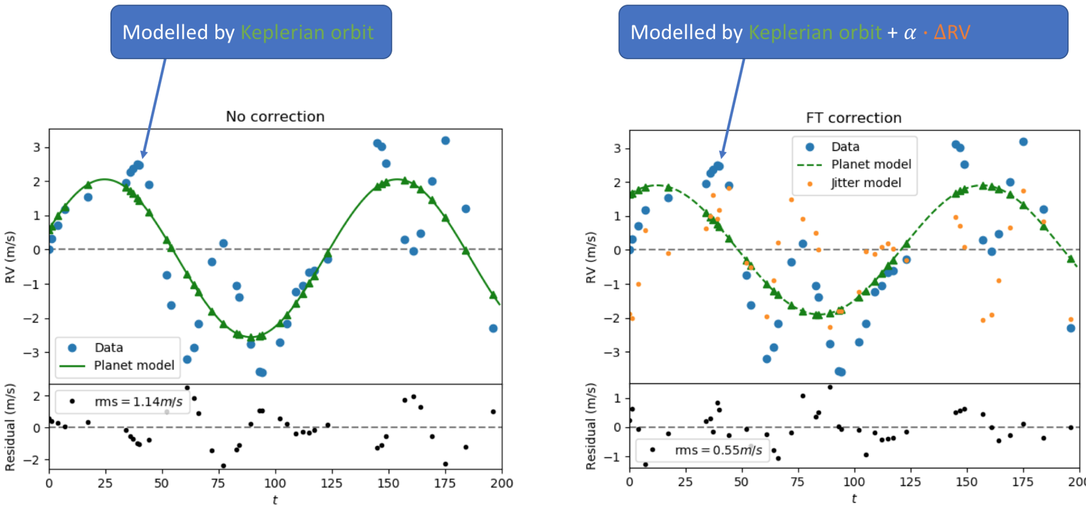

Fig. 2.16: Radial velocity fitting. Theses are two fittings that comes out from the MCMC corner plots in Fig. 2.15. On the left panel without jitter correction, we can see that the input jitter increases the scatter of the raw radial velocities, resulting in an overestimated amplitude A; while on the right panel with jitter correction, the additional input jitter is accounted for by the jitter model.

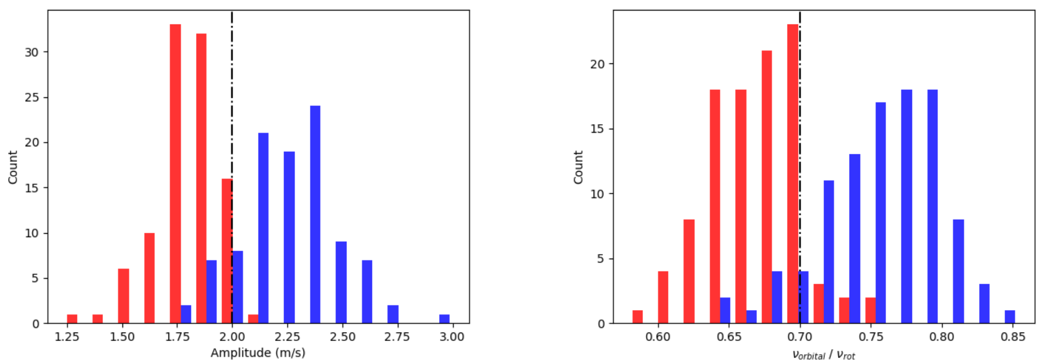

(a) **(b)**

Fig. 2.17: Distribution of recovered parameters. The red are results of jitter correction by Fourier transform; The blue are results of no jitter correction.

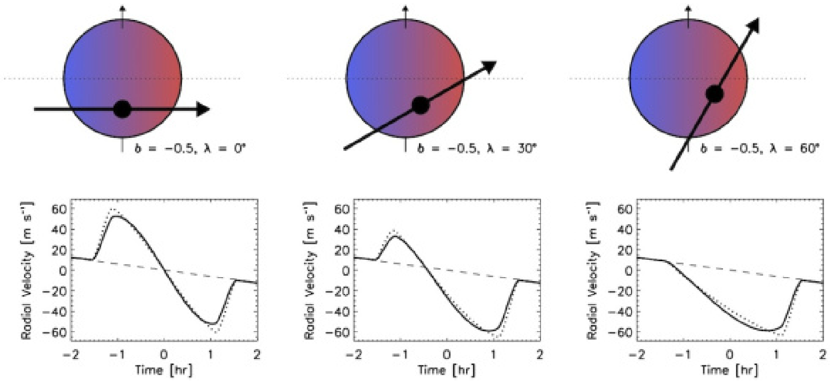

Fig. 2.18: Demo: Rossiter–McLaughlin effect (reference...). It is a apparent radial velocity change of the parent star due to an eclipsing binary (whether star or planet) that breaks the observed flux symmetry in the stellar photosphere, resulting in imbalanced redshift and blueshift. It shows in this plot three different star-planet alignments that causes three corresponding different shapes of radial velocity curve, and hence the radial velocity curve sheds information on the geometry of the alignment.

2.3 Fourier transform with real observations

2.3.1 HD189733: Rossiter–McLaughlin effect as jitter

HD189733 is a well studied binary star system. The main star HD189733 A is known to host a gas giant exoplanet HD189733 b, first detected by transits (reference...) and later by Doppler spectroscopy (references...). It was also the first exoplanet transit observed in X-ray (references...).

We choose this target for the following reasons:

- The exoplanet is well confirmed;
- The host star is bright enough: $m_V = 7.66$;
- The gas giant exoplanet causes a prominent apparent radial velocity while it transits (~ 40 m/s) due to Rossiter–McLaughlin effect.

We treat as if it were an "active" star with one big dark starspot, as the Rossiter–McLaughlin effect causes the line profile deformed in a similar manner that a starspot would do (Fig. 2.18). We aim to test if our jitter model can account for the radial velocity variation from Rossiter–McLaughlin effect.

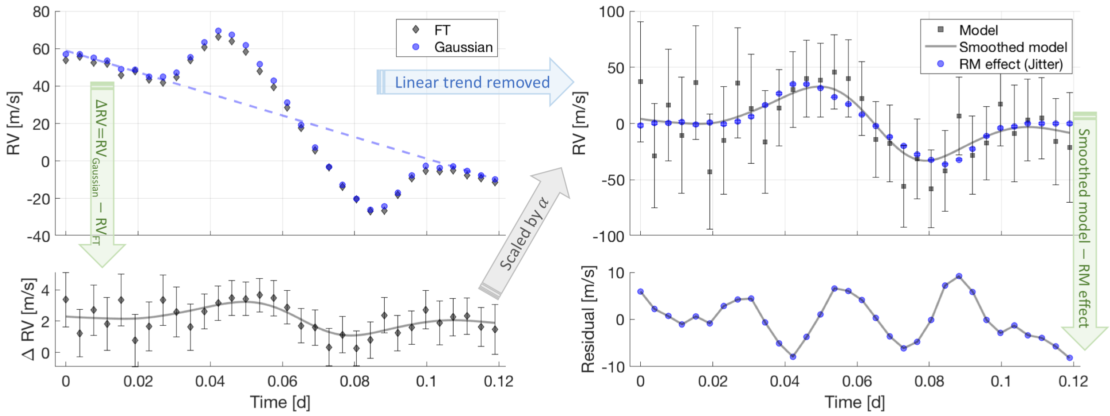

Fig. 2.19: HD189733: removal of Rossiter–McLaughlin effect as jitter. From RV_{Gaussian} and RV_{FT} to ΔRV. The scattered ΔRV are smoothed by applying a moving average with a Gaussian filter and further weighted according to the size of errorbar. It is then scaled by α to match the jitter (in this case the radial velocities of the observed Rossiter–McLaughlin effect). The residual is the difference between the smoothed jitter model and the observed Rossiter–McLaughlin effect. Errorbars are not plotted for the residuals for the reason that they will overwhelm the residual themselves.

The procedure is rather standardized. Both RV_{Gaussian} and RV_{FT} are calculated from the HARPS cross-correlation functions of the spectra. $\Delta RV = RV_{\text{Gaussian}} - RV_{\text{FT}}$ are then smoothed by a Gaussian filter. The prototype of the Rossiter–McLaughlin radial velocity curve is already identifiable (ΔRV of the lower panel of Fig. 2.19).

During transit, as the parent star and the exoplanet are along the line of sight, there will be no contribution to radial velocity by the orbiting exoplanet. However, the radial velocity shows an inclined trend in this system. It is due to the other orbiting star in the binary star system. Considering the orbital period of the binary star estimated around 3,200 years (reference...), the radial velocity contribution from the other star during the timespan of transit (~ 0.08 days) can be treated linear. By removing such a linear trend, which is fitted for the non-transiting part, we can extract the observed Rossiter–McLaughlin radial velocity curve. It is treated as jitter and modelled by $\alpha{\cdot}\Delta RV$ (Fig. 2.19 upper right). Note that the errorbars of the jitter model also becomes a factor of α ($\alpha \gg 1$) larger; however, the model itself shows a descent approximation of the Rossiter–McLaughlin radial velocity curve. The difference between our modelled jitter and the observed Rossiter–McLaughlin effect peaks at ~ 10 m/s, a $\sim 75\%$ removal of the jitter from ~ 40 m/s.

Remarks The effective length of the smoothing kernel should be carefully chosen. In this case, it's chosen most effective within roughly one neighbouring data point on both size. While mitigating the effect of noise (especially for relatively lower S/N data outside the transits), to which the Fourier transform is sensitive, it also smears the drastic velocity change when the planet ingresses and egresses the stellar disk. To solve this awkward situation, an adaptive (i.e. S/N dependent) effective length of the smoothing kernel may be used.

2.3.2 Examples 2

HD 49933 is an F2 main sequence star with an apparent magnitude of $m_V = 5.8$ ([2]),

2.3.3 Example 3

A float barrier will stop figures from going beyond this point. They are handy to make sure they don't go into the next section.

2.4 References

[1] X. Dumusque, I. Boisse, and N. C. Santos. Soap 2.0: A tool to estimate the photometric and radial velocity variations induced by stellar spots and plages. *The Astrophysical Journal*, 796(2):132, 2014. 7

[2] S. Malaroda. Study of the F-type stars. I. MK spectral types. *aj*, 80:637–641, August 1975. 27